



# Hot Deformation Behavior and Processing Map of a Fe-11Mn-10Al-0.9C Duplex Low-Density Steel Susceptible to $\kappa$ -Carbides

Degang Liu, Hua Ding, Minghui Cai, and Dong Han

(Submitted January 23, 2019; in revised form May 17, 2019; published online July 17, 2019)

The hot deformation behavior of a Fe-11Mn-10Al-0.9C duplex low-density steel has been investigated, based on a series of isothermal compression tests at temperatures of 800–1100 °C and strain rates of 0.001–10 s<sup>-1</sup>. At relatively lower temperatures, with austenite decomposing, continuous dynamic recrystallization of ferrite and the formation of inter-granular  $\kappa$ -carbide were responsible for significant softening. At high deformation temperature where austenite was a dominant phase, dynamic recrystallization (DRX) is the restoration mechanism. Processing maps were developed at different plastic strains employing dynamic materials model and further verified through microstructural characterization. The optimal hot deformation condition at a large strain (0.7) was identified as deformation temperature of 950–1100 °C and strain rate of 0.01–1.0 s<sup>-1</sup>. In this domain, the original coarse grains could be replaced by the fine and uniform recrystallized grains, indicating that the high efficiency was dissipated by DRX. Meanwhile, two instable regions resulted from the formation of inter-granular  $\kappa$ -carbides and necklace structure should be avoided during hot processing.

**Keywords**  $\kappa$ -carbide, duplex low-density steel, dynamic recrystallization, processing map

## 1. Introduction

Recently, a newly developed medium-Mn low-density duplex (austenite + ferrite) steel has drawn increasing attraction due to its excellent mechanical properties and remarkable density reduction, as well as the lower production cost when compared with the traditional high-Mn high-Al austenitic steels (Ref 1–11). Accordingly, some preliminary studies on composition design (Ref 1, 2), microstructural evolution (Ref 3) and phase transformation (Ref 4) related to medium-Mn low-density steels have been extensively performed, aiming to obtain the promising overall mechanical properties at ambient temperature.

In general, the  $\kappa$ -carbide (a type (Fe,Mn)<sub>3</sub>AlC with a perovskite structure) has been actively utilized to enhance the yield strength of Al-containing low-density steels (Ref 1, 5). The structure of  $\kappa$ -carbide is based on the face-centered-cubic crystal lattice, and the elemental site-occupancy of the  $\kappa$ -carbide is such that: with C atoms at the body-centered sites, Fe/Mn atoms randomly at the face-centered sites, and Al atoms at the cornered sites (Ref 6, 7). According to the composition and heat treatment,  $\kappa$ -carbides show different characteristics: (1) nano-sized intra-granular shearable  $\kappa$ -carbides coherent to

the austenite matrix could enhance the strength without deteriorating the ductility (Ref 6–8); (2) the coarse lamellar inter-granular  $\kappa$ -carbides are prone to induce an embrittlement (Ref 9, 10).

In addition to the inherent properties of low-density steels, hot deformation may alter their flow behavior and precipitation behavior, eventually influencing the room temperature microstructures and mechanical properties of the materials. The recent research on the hot isothermal compression of a Fe-21Mn-11Al-1.5C-2Si austenite-based steel revealed the occurrence of discontinuous dynamic recrystallization (DDRX) and dynamic precipitation of intra-granular  $\kappa$ -carbides (Ref 12). In the duplex-structure manganese steels, the coexistence of austenite and ferrite could result in complicated flow behavior and may bring adverse effect in hot workability, owing to the difference in thermal expansion coefficients and deformation responses between different phases (Ref 13–16). Moreover, it was found that strain transferred from softer ferrite to harder austenite during further deformation, leading to the pronounced microstructural inhomogeneity, especially in the interphase regions (Ref 13, 14, 17). Mohamadizadeh et al. developed 3D processing maps of a Fe-18Mn-8Al-0.8C duplex steel, demonstrating the safe and unsafe deformation conditions in association with the microstructural evolution (Ref 16). In Fe-Mn-Al-C quaternary alloy system, the increasing amount of C and Al together with the decreasing Mn content could facilitate the precipitation of both inter/intra-granular  $\kappa$ -carbides, and thus medium-Mn low-density steels usually undergo hot working in the ferrite + austenite +  $\kappa$  phase region (Ref 12, 18). The fraction, morphology, size and localization of  $\kappa$ -carbides would have a great impact on the hot deformation of low-density steels. To our best knowledge, the precipitation behavior of  $\kappa$ -carbide during hot deformation and its influence on hot workability of medium-Mn low-density steels have not been documented so far.

Therefore, the present work was aimed to study the hot flow behavior and microstructural evolution of a novel fer-

Degang Liu, Hua Ding, Minghui Cai, and Dong Han, School of Materials Science and Engineering, Northeastern University, Shenyang 110819 Liaoning Province, China; and Key Laboratory of Lightweight Structural Materials, Shenyang 110819 Liaoning Province, China. Contact e-mails: dingh@smm.neu.edu.cn and cmhing@126.com.

rite + austenite +  $\kappa$ -carbide structure Fe-11Mn-10Al-0.9C low-density steel. The emphasis was placed on a fundamental understanding of deformation mechanisms related to deformation temperature (800–1100 °C) and strain rate (0.001–10 s<sup>-1</sup>). The processing map, originally proposed by Raj (Ref 19), was developed as well to gain the optimum processing regions, together with microstructural verification.

## 2. Experimental

The medium-Mn duplex low-density steel with a composition of Fe-11Mn-10Al-0.9C was prepared by vacuum induction melting. The 50 kg ingot was forged at 1200 °C and then hot-rolled after homogenization at 1200 °C for 2 h to the thickness of 12 mm with a reduction of 70%. Cylindrical specimens, 15 mm in height and 8 mm in diameter, were machined from the hot-rolled slab with the longitudinal axis parallel to the rolling direction. The isothermal compression tests were carried out on a Gleeble-1500 thermo-mechanical simulator at deformation temperatures of 800–1100 °C with interval of 50 °C and strain rates of 0.001–10 s<sup>-1</sup> with interval of an order of magnitude, respectively. Before compression tests, all cylindrical specimens were heated at a rate of 30 °C/s to 1250 °C, soaked for 240 s, then cooled to various deformation temperatures at 20 °C/s and held for 30 s for temperature homogenization. Molybdenum foils were applied on both the contact surfaces of specimens to reduce the friction during hot compression testing. All specimens were deformed to a strain of 0.7 and then immediately quenched into water to remain the hot deformation microstructures.

Microstructures were observed using an OLYMPUS DSX500 optical microscopy (OM) and scanning electron microscopy (SEM). All specimens for OM and SEM were sliced along the compression axis and then performed by standard mechanical and electrochemical polishing methods. Specimens were etched in a solution of 2.8 mL hydrochloric acid, 100 mL methanol and 4 g picric acid. Electron backscattered diffraction (EBSD) was carried out in this SEM operated at 15 kV with a step size of 0.8  $\mu$ m for typical deformed specimens. The EBSD mappings were visualized and post-processed using HKL Channel 5 software. The transition angle between low- and high-angle grain boundaries (LAGBs/HAGBs) was established as  $\theta = 15^\circ$  (Ref 20). Tecnai G<sup>2</sup> 20 transmission electron microscopy (TEM) was used to investigate the fine microstructure and precipitation behavior. TEM specimens were electropolished by using 9% perchloric acid in methanol at -30 °C. Phase constituents were identified by x-ray diffraction (XRD, Rigaku, D/Max2250/PC) with Cu-K $\alpha$  radiation ( $\lambda = 1.5405 \text{ \AA}$ ). The specimens were Zeiss Ultra Plus scanning scanned in the angle range of 40–100° with a speed of 2°/min.

## 3. Results and Discussion

### 3.1 Equilibrium Phase Diagram and Initial Microstructure

The phase diagram of Fe-11Mn-10Al-0.9C steel was calculated by Thermo-Calc software with database TCFE7. The phase fractions in equilibrium are shown in Fig. 1. As the temperature decreased from 1100 to 855 °C, the phase fraction

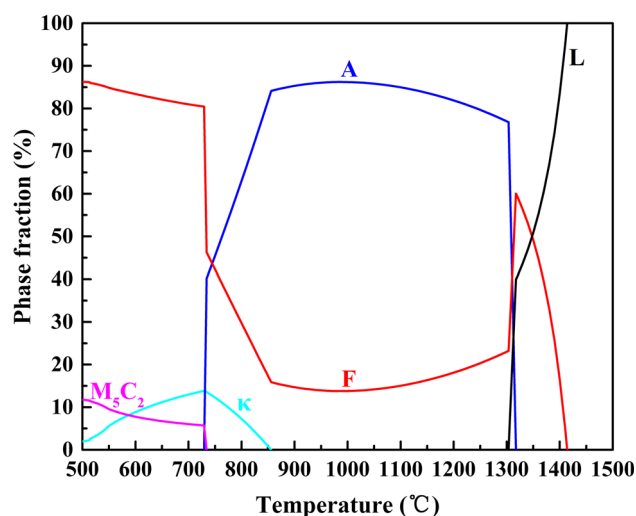


**Fig. 1** Equilibrium phase diagram of Fe-11Mn-10Al-0.9C steel calculated by the Thermo-Calc software. (ferrite (F), austenite (A) and  $\kappa$ -carbide ( $\kappa$ ))

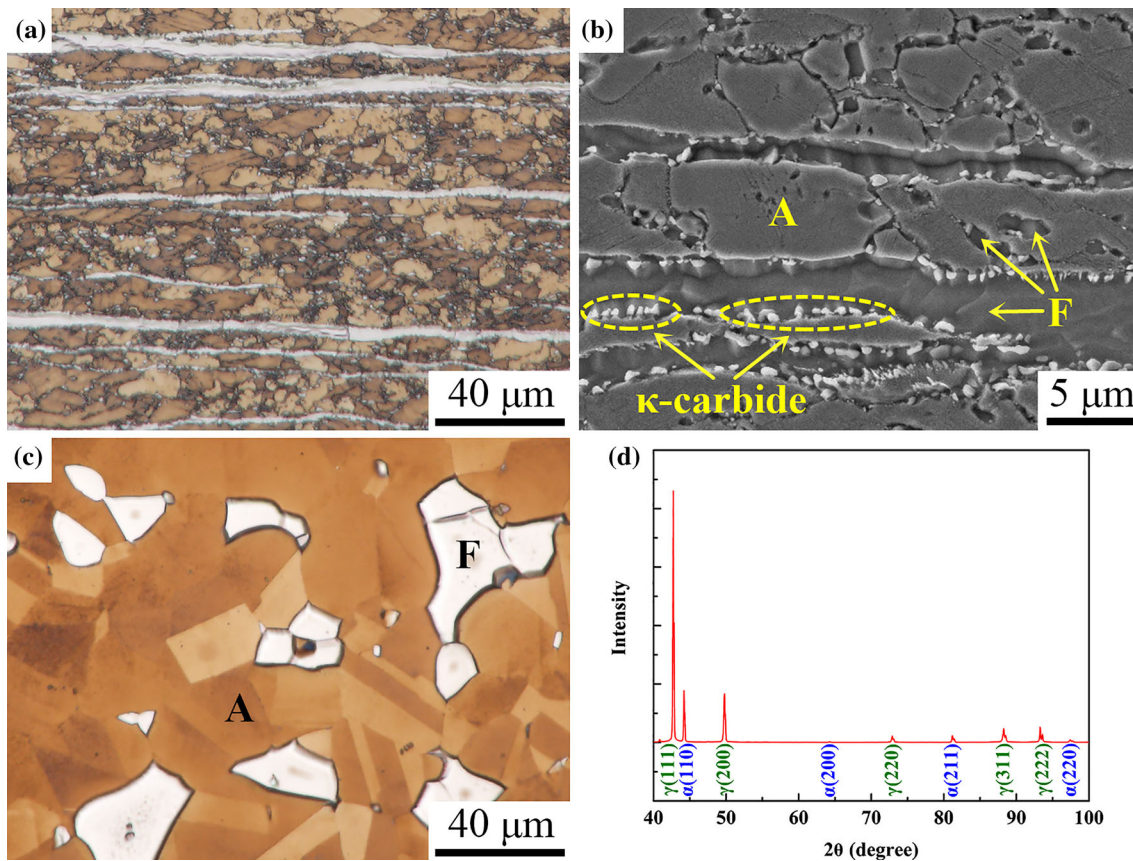
of ferrite first dropped and then increased, with a minimum at 990 °C. At 855 °C, the  $\kappa$ -carbide began to form by eutectoid reaction (austenite  $\rightarrow$  ferrite +  $\kappa$ -carbide) (Ref 2), followed by the abrupt drop of the amount of austenite.

The initial microstructure of the hot-rolled steel (Fig. 2a) shows a typical banded structure of ferrite (white) and austenite (dark yellow) parallel to the rolling direction, in conjunction with some fine ferrite at austenite boundaries. Also, some  $\kappa$ -carbide particles were observed nearby the interface of austenite and ferrite as well as the austenite boundaries (Fig. 2b). After soaking at 1250 °C for 240 s, the optical micrograph demonstrates the isolated island-like ferrite embedded into the austenite matrix (Fig. 2c and d). The fraction of austenite was about 89%, and the average grain size of austenite and ferrite was  $49.2 \pm 19.5 \mu\text{m}$  and  $20.4 \pm 14.2 \mu\text{m}$ , respectively.

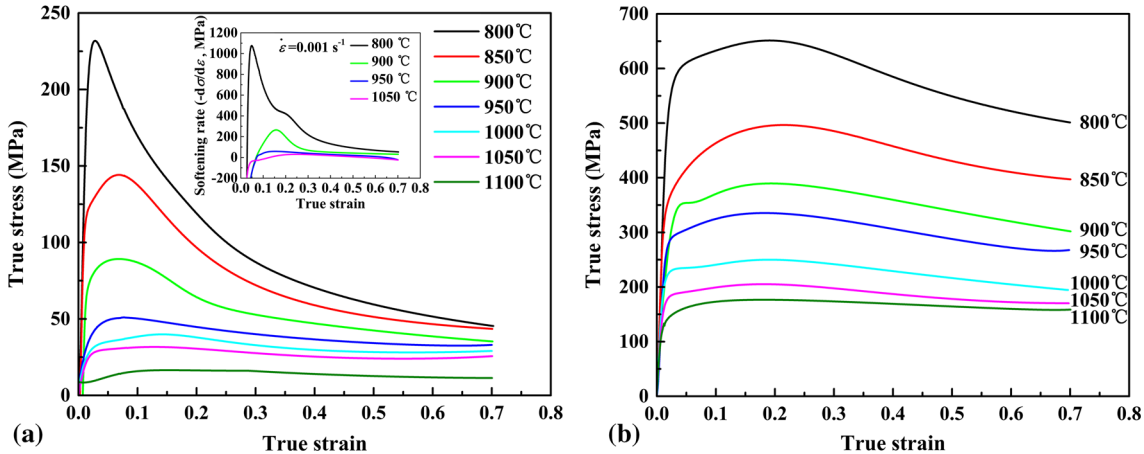
### 3.2 True Stress–True Strain Curves

Figure 3 shows the true stress–true strain curves obtained from hot compression tests at strain rates of 0.001–10 s<sup>-1</sup> under various deformation temperatures. The flow stress is sensitive to both deformation temperature and strain rate. As was commonly observed that with increasing strain rate or dropping deformation temperature, the peak stress level was elevated.

Based on the flow behavior, the present flow curves could be classified into the following two categories: (1) At relatively lower deformation temperatures ( $\leq 900 \text{ }^\circ\text{C}$ ), the flow stress increased sharply during initial work hardening stage of deformation until it reached the peak points, and then decreased rapidly with increasing strain, suggesting the occurrence of dynamic softening behavior (dynamic recovery or dynamic recrystallization (DRV/DRX)) (Ref 21). The flow curves showed an extensive softening without any steady state, which may be also associated with the strain-induced dynamic transformation from austenite to ferrite and  $\kappa$ -carbide (Ref 22). (2) At higher deformation temperatures ( $\geq 950 \text{ }^\circ\text{C}$ ), flow stress decreased gradually with true strain after peak stress, reaching a final steady state, indicating a typical DRX of the austenite during deformation (Ref 21). These two cases were in accordance with the variation of softening rate ( $-d\sigma/d\varepsilon$ ), as



**Fig. 2** (a) OM and (b) SEM micrographs of hot-rolled specimen, (c) OM micrograph and (d) XRD profiles of the specimen after soaking at 1250 °C for 240 s (A: austenite, F: ferrite)



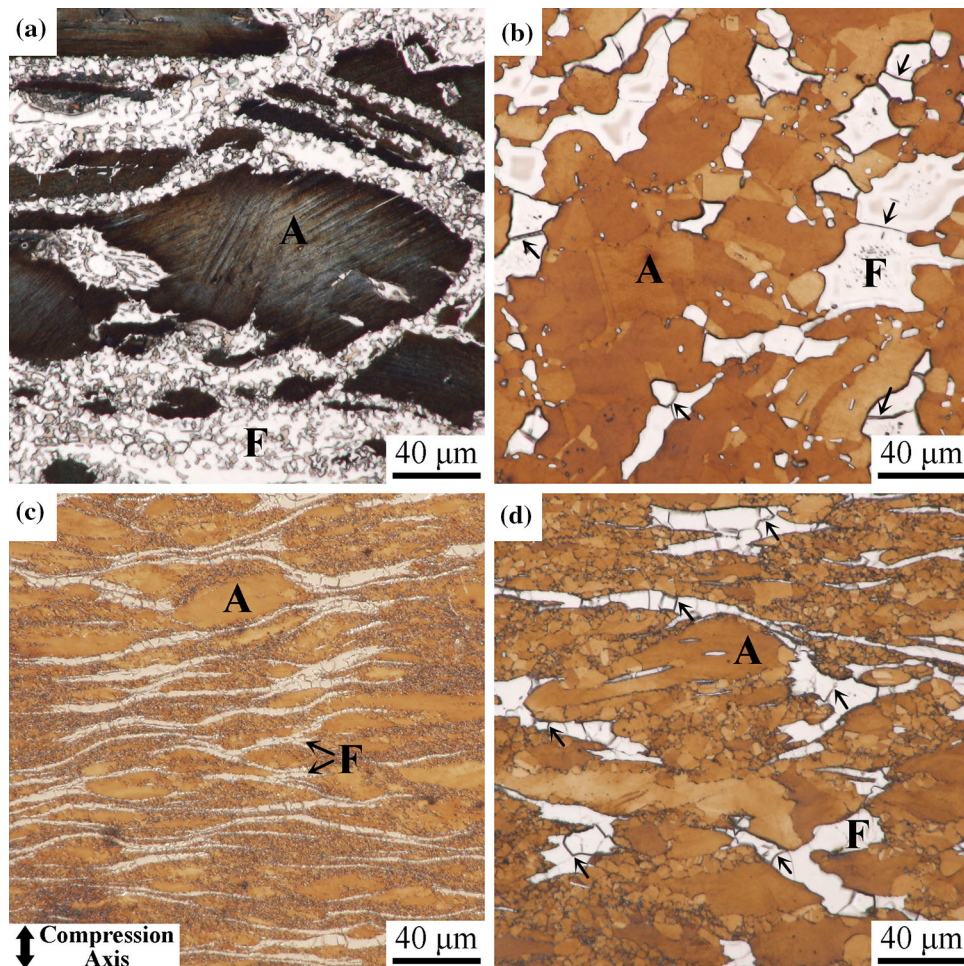
**Fig. 3** True stress–true strain curves obtained at strain rate of (a)  $0.001 \text{ s}^{-1}$  and (b)  $10 \text{ s}^{-1}$ , and the variation of softening rate of samples deformed at  $0.001 \text{ s}^{-1}$  inserted in (a)

illustration inserted in Fig. 3(a). Accordingly, the detailed microstructural investigation was performed to further reveal the underlying deformation mechanism in the following section.

### 3.3 Hot Deformation Microstructure

Figure 4 shows the deformed microstructures corresponding to these two types of flow curves. When the specimen was

deformed at 800 °C, the severely pancaked prior austenite and ferrite grains were observed (Fig. 4a and c). In Fig. 4(a), obvious slip traces were observed in the austenite grains, along with some inter-granular  $\kappa$ -carbide particles around the ferrite grains. With increasing strain rate to  $10 \text{ s}^{-1}$ , some amount of new small grains appeared nearby the deformed austenite grains (Fig. 4c), which was called the necklace structure (Ref 23). The preferential nucleation of DRX in polycrystals was found to proceed predominantly at the prior grain boundaries and



**Fig. 4** OM micrographs corresponding to two types flow curves with specimens deformed at (a, c) 800 °C and (b, d) 1050 °C (a and b for 0.001 s<sup>-1</sup>, c and d for 10 s<sup>-1</sup>) (A: austenite, F: ferrite)

expand into the unrecrystallized volume (Ref 24). Figure 4(b) and (d) shows the microstructure deformed at temperature of 1050 °C corresponding to the second type of flow curves. The delineated boundaries in ferrite (marked by arrows) and the sharper austenitic boundaries with twins were observed, which are typical of continuous dynamic recrystallization (CDRX) in ferrite and DRX in austenite (Ref 25).

In order to study the microstructural evolution at different hot deformation stages, the deformed specimens were interrupted at different strain levels (0.05, 0.2, 0.4 and 0.7) under the deformation condition of 800 °C and 0.001 s<sup>-1</sup>. As shown in Fig. 5, the  $\kappa$ -carbides first appeared along the phase interface of austenite and ferrite and austenite boundaries (Fig. 5a). At true strain of 0.2, the  $\kappa$ -carbides were nucleated preferentially at the lattice defects (Fig. 5b), such as deformation bands and annealing twin boundaries. As the strain amount increased to 0.4, the eutectoid reaction occurred, causing the formation of ferrite and  $\kappa$ -carbides within the austenite matrix. With further increasing strain to 0.7, the volume fraction of austenite dropped to ~ 28 from 90% at solution condition (Table 1), thus indicating that ferrite became a dominant phase under low temperature and heavy deformation conditions, especially at lower strain rates.

Fine microstructure characterization was further conducted using TEM for the deformed specimens at true strain of 0.05, 0.2

and 0.7 under the deformation condition of 800 °C and 0.001 s<sup>-1</sup>, as shown in Fig. 6. At the true strain of 0.05, the dislocation walls (DWs) were dominantly observed in Fig. 6(a), which indicates an activation of DRV giving rise to the dislocation rearrangement and annihilation within ferrite phase (Ref 26). At the true strain of 0.2, the ferrite was evolved by the subgrain boundary structure made up of the high-density dislocation tangle (Fig. 6b). With further straining to 0.7, some new almost equiaxed grains with HABs were formed by the progressive rotation of subgrains (Ref 17) (Fig. 6c). In this process, the low-angle boundaries (LABs) created by DRV at the early stage of deformation converted into high-angle boundaries (HABs) through continuous absorption of dislocations during straining (Ref 17). The formation of new grains without obvious nucleation and growth sequence was termed CDRX, which was reported to operate during hot deformation of ferrite for single- and dual-phase steels (Ref 17, 27). With increasing strain, a significant softening behavior was closely associated with the strain transforming from austenite into ferrite, the occurrence of CDRX in ferrite together with the strain-induced dynamic transformation related to the formation of  $\kappa$ -carbides.

As shown in Fig. 7(a), the  $\kappa$ -carbides formed by the eutectoid reaction coarsened to ~ 1-3.8  $\mu\text{m}$  during hot deformation condition of 800 °C/0.001 s<sup>-1</sup>, which could be considered as isothermal aging at this temperature for 700 s (Ref 12).

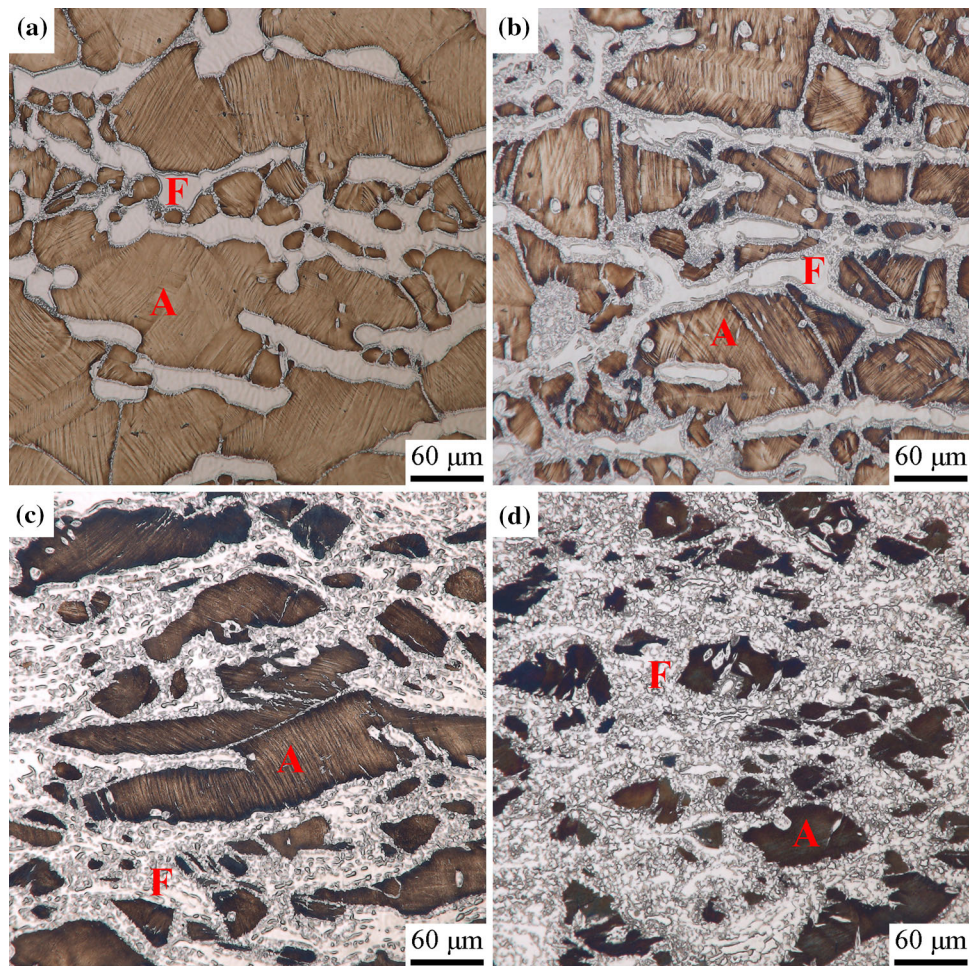


**Fig. 5** Austenite gradually decomposing into ferrite and  $\kappa$ -carbide with strain increasing, illustrated by OM micrographs of specimens deformed at 800 °C and 0.001 s<sup>-1</sup> at different strains of (a) 0.05, (b) 0.2, (c) 0.4 and (d) 0.7 (A: austenite, F: ferrite)

**Table 1** Austenite volume fraction as a function of deformation degree at 800 °C and 0.001 s<sup>-1</sup>

Deformation degree	ST	0.05	0.2	0.4	0.7
Fraction (%)	89.62 ± 0.7	80.63 ± 1.1	58.56 ± 1.7	44.97 ± 1.3	27.89 ± 2.1

ST solution treatment. Four representative optical micrographs (1194 × 1194 pixel) of each sample were used to measure the fraction of austenite, based on the pixel method by the image analysis software (Image Pro Plus 6.0)

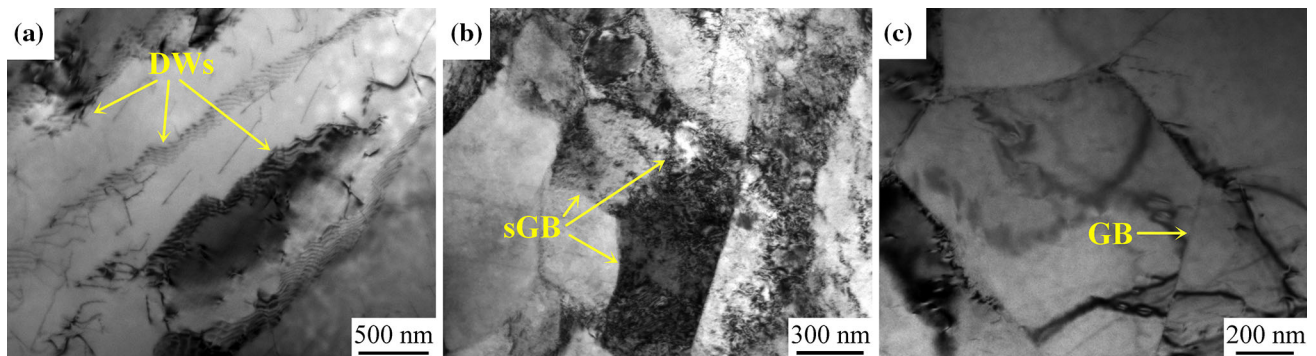


**Fig. 6** The microstructural evolution of ferrite through CDRX characterized by TEM micrographs of the specimen deformed at 800 °C and 0.001 s<sup>-1</sup> (a) 0.05, (b) 0.2 and (c) 0.7 (DWs: dislocation walls, sGB: subgrain boundary, GB: grain boundary)

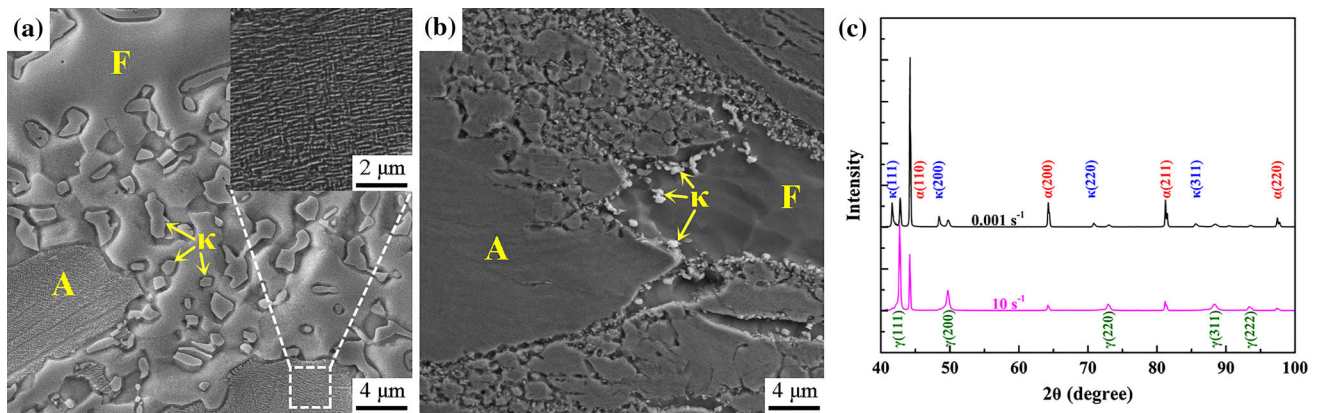


**Fig. 7** The formation of inter-granular  $\kappa$ -carbide particles at the low deformation temperatures as indicated by SEM micrographs of specimens deformed at (a) 800 °C and  $0.001 \text{ s}^{-1}$  with feature of intra-granular  $\kappa$ -carbide inserted, (b) 800 °C and  $10 \text{ s}^{-1}$ , and (c) the corresponding XRD pattern (A: austenite, F: ferrite,  $\kappa$ :  $\kappa$ -carbide)

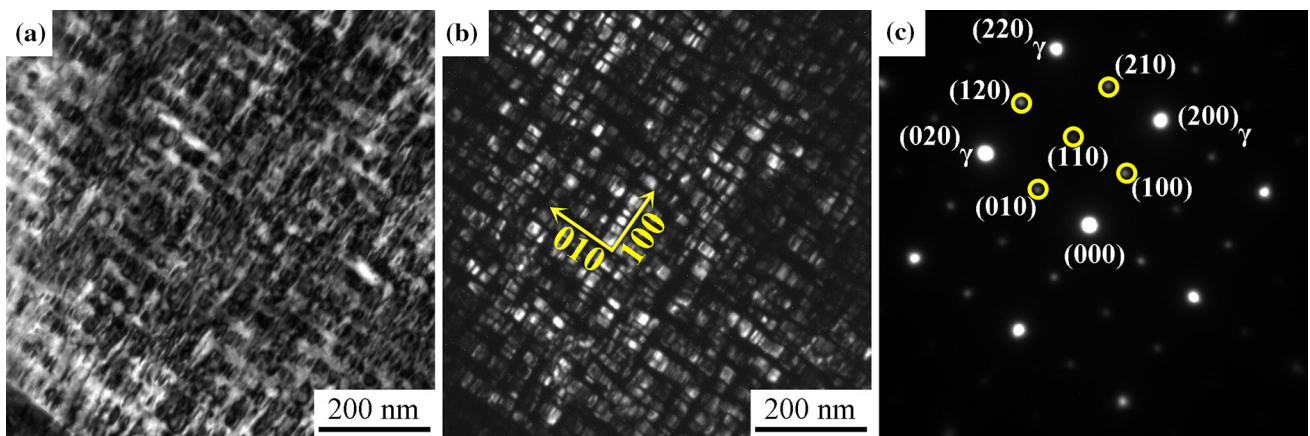


**Fig. 8** The formation of intra-granular  $\kappa$ -carbide showed by TEM micrographs of the specimen deformed at 800 °C and  $10 \text{ s}^{-1}$ , (a) bright field, (b) dark field and (c) selected area diffraction pattern from the [001] austenite

In addition to the coarsening of inter-granular  $\kappa$ -carbide particles, the typical modulated cuboidal  $\kappa$ -carbides of  $\sim 100 \text{ nm}$  were also observed in the austenite, as illustrated by an insert in Fig. 7(a). At the strain rate of  $10 \text{ s}^{-1}$ , some amount of inter-granular  $\kappa$ -carbides with smaller size was mixed in the ultrafine austenite DRX grains (Fig. 7b).

The x-ray diffraction patterns of the specimens deformed at 800 °C are provided in Fig. 7(c). All peaks of austenite, ferrite and  $\kappa$ -carbide were detected for the specimen strained at  $0.001 \text{ s}^{-1}$ , while no peaks of  $\kappa$ -carbides appeared for the specimen strained at  $10 \text{ s}^{-1}$ . This may be because of the small volume fraction of nano-sized  $\kappa$ -carbides in the latter specimen, in view of the accuracy of macro-XRD measurements. Alternatively, some nanoscale  $\kappa$ -carbide particles were observed in austenite for the specimen strained at  $10 \text{ s}^{-1}$  using TEM (Fig. 8). It has been shown that  $\kappa$ -carbides exhibit a rectangular morphology with a  $\{001\}$  habit plane (Fig. 8b), which was thought to be formed through the spinodal decomposition (Ref 6, 7). Meanwhile, the preferential growth direction of  $\kappa$ -carbides was mainly attributed to the rather large increase in the elastic misfit with increasing holding time (Ref 7). The kinetics of ordered  $\kappa$ -carbides may be further enhanced by the pre-existence of a favorably stress field during hot deformation (Ref 6, 12).

### 3.4 Processing Map

**3.4.1 Processing Map Development.** Processing maps have been used to evaluate the hot deformation characteristics of a wide range of metallic materials such as magnesium alloys, titanium alloys, Ni-base superalloys and stainless steels (Ref 19-21, 25, 28-33). In general, materials were considered to be power dissipater of energy, based on the DMM. The power dissipation ( $P$ ) at a certain deformation condition, i.e., deformation temperature and strain rate involved the following two parts: (1) part  $G$  representing the power dissipated by plastic work; (2) part  $J$  related to the dynamic microstructural changes (Ref 20, 25, 29, 30), which can be expressed as a function of flow stress ( $\sigma$ ), strain ( $\epsilon$ ) and strain rate ( $\dot{\epsilon}$ ):

$$P = \sigma \dot{\epsilon} = G + J = \int_0^{\dot{\epsilon}} \sigma d\dot{\epsilon} + \int_0^{\sigma} \dot{\epsilon} d\sigma \quad (\text{Eq 1})$$

The power partitioning between  $G$  and  $J$  was equal to the strain rate sensitivity index ( $m$ ), which can be defined as:

$$m = \frac{dJ}{dG} = \frac{\dot{\epsilon} d\sigma}{\sigma d\dot{\epsilon}} = \frac{\partial(\log \sigma)}{\partial(\log \dot{\epsilon})} \quad (\text{Eq 2})$$

Meanwhile, microstructure-related term could be sharpened by normalizing the  $J$  with the total power input ( $\sigma, \dot{\epsilon}$ ) where an

ideal linear dissipater had an  $m$  value equal to 1. Accordingly, a dimensionless parameter which was called the efficiency of power dissipation ( $\eta$ ) was given as:

$$\eta = \frac{(dJ/dP)}{(dJ/dP)_{\text{linear}}} = \frac{J}{J_{\text{max}}} = \frac{2m}{m+1} \quad (\text{Eq 3})$$

The power dissipation map could be constructed by plotting the  $\eta$  against deformation temperature and strain rate. Different domains in the 2D contour map represented various microstructural mechanisms. Furthermore, domains of flow instability were demarcated based on the following Prasad's (Ref 31) instability criterion  $\zeta(\dot{\epsilon})$ :

$$\zeta(\dot{\epsilon}) = \frac{\partial \log[m/(m+1)]}{\partial \log(\dot{\epsilon})} + m < 0 \quad (\text{Eq 4})$$

The variation of  $\zeta(\dot{\epsilon})$  with deformation temperature and strain rate was usually plotted as contour lines, which was called as an instability map where  $\zeta(\dot{\epsilon})$  was negative.

Thus, processing maps could be established by superimposing the instability maps over the power dissipation maps. The values against each contour represent the efficiency of power dissipation as percent, and the shallow regions corresponded to the unstable hot deformation domains. Figure 9 shows the obtained processing maps of the Fe-11Mn-10Al-0.9C duplex low-density steel at different strains of 0.1, 0.2, 0.4 and 0.7. All processing maps exhibited two domains with peak

efficiency ( $\geq 42\%$ ), corresponding to the low strain rates and high deformation temperatures (Domain I and Domain II). There also existed two instability areas  $A$  and  $B$  located at the top-left corner and top-right corner of these processing maps.

At the true strain of 0.1 (Fig. 9a), an efficiency domain I was located in the temperature range of 800-1000 °C and lower strain rates, i.e., less than  $0.003 \text{ s}^{-1}$ . After straining to 0.2 (Fig. 9b), domain I expanded to  $0.01 \text{ s}^{-1}$  and the efficiency of power dissipation was increased to 61%. An increase in the peak efficiency with strain was probably caused by the dissolution or growth of precipitates, phase transformations or wedge cracking (Ref 34, 35). At the true strain of 0.1 and 0.2, domain II was at the strain rates below  $0.03 \text{ s}^{-1}$  and deformation temperatures above 1080 °C. As the true strain was increased to 0.4 and 0.7 (Fig. 9c and d), domain II was shifted to a higher strain rate and a lower deformation temperature region. It was worth noting that the efficiency of power dissipation in the original domain II decreased gradually instead of increasing continuously with strain. It was speculated that the decline of efficiency was attributed to the abnormal grain growth due to the long dwell time at high temperatures and the strain rate of  $0.001 \text{ s}^{-1}$  (Ref 33). The instability area  $A$  remained constant through the whole deformation process. On the contrary, the instability area  $B$  expanded to a greater scope with imposing more strain. Therefore, the processing window of the present Fe-11Mn-10Al-0.9C steel shrunk to a narrower region with increasing strain.

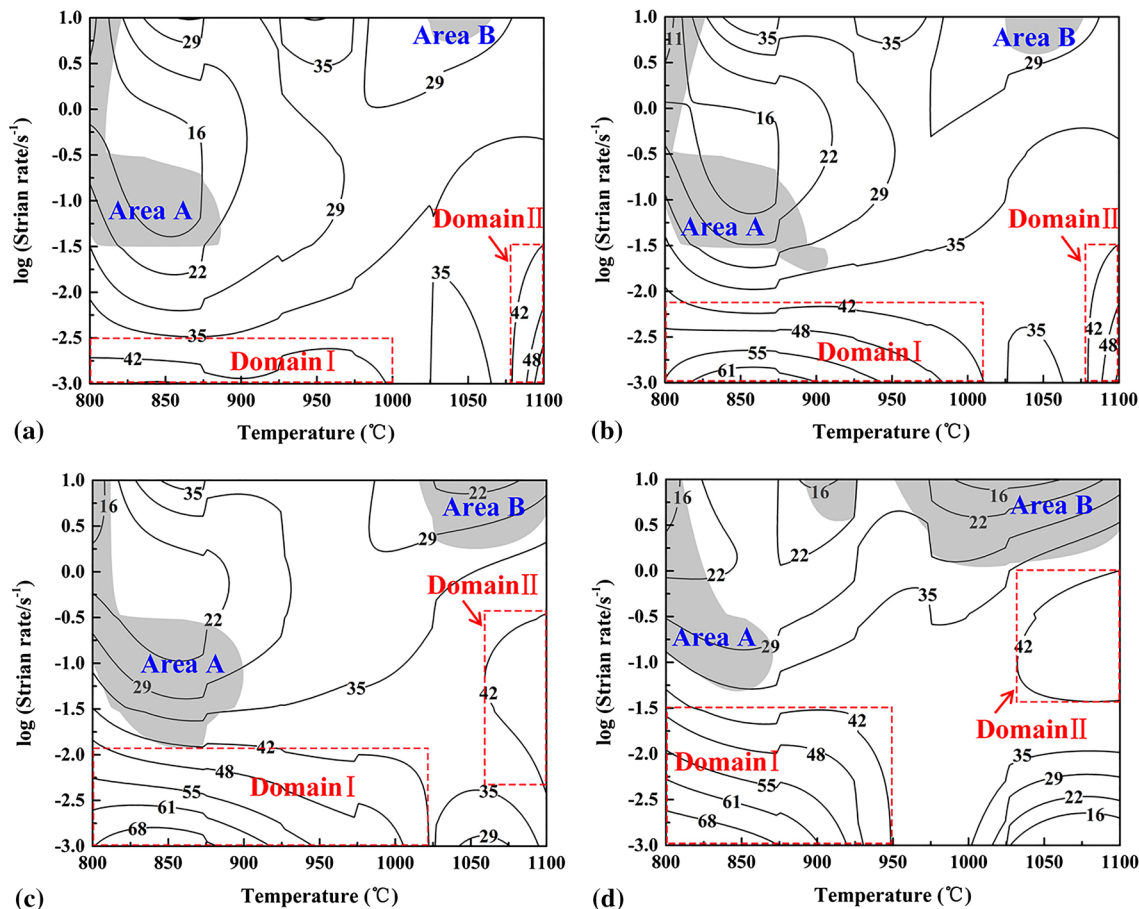


**Fig. 9** Processing maps of Fe-11Mn-10Al-0.9C steels at different strains of (a) 0.1, (b) 0.2, (c) 0.4 and (d) 0.7. The contour number represents the efficiency of power dissipation ( $\eta$ ). The gray region corresponds to the instability region

**3.4.2 Verification of Workability by Microstructural Observation.** Each efficiency domain and instability area can be interpreted based on the dominant deformation mechanisms associated with microstructural characteristics. Taking the specimen deformed at true strain of 0.7 as an example, the typical domains were determined and the corresponding microstructure analyses were used to validate the prediction in processing maps.

Domain I corresponded to the deformation temperatures between 800 and 950 °C and the strain rates lower than  $0.03 \text{ s}^{-1}$ . This domain exhibited the highest efficiency under all deformation conditions. The microstructure of the specimen deformed at 800 °C and  $0.01 \text{ s}^{-1}$  corresponding to domain I is shown in Fig. 10(a). Fine  $\kappa$ -carbide particles with size of 0.3–1.2  $\mu\text{m}$  were observed to distribute along the phase interface between austenite and ferrite, which was consistent with the high efficiency of 55%. At the lower strain rate of  $0.001 \text{ s}^{-1}$ , the final microstructure was composed of the duplex phase matrix (austenite and ferrite), together with the lamellar structure consisting of fine ferrite,  $\kappa$ -carbide and retained austenite formed along the prior austenite grain boundaries, as marked by white ellipses in Fig. 10(b). The high partitioning of Al atoms to austenite together with the fast diffusion of C greatly accelerated the decomposition of austenite and the formation of needle-like  $\kappa$ -carbides (Ref 36). The formation of lamellar structure and coarsening of  $\kappa$ -carbides gave rise to an increasing efficiency over 68%. The specimen deformed at a lower temperature (Fig. 10a) exhibited fine and intense microband structure in austenite implying the flow localization on the dense slip plane  $\{111\}$  (Ref 11, 16).

The typical microstructure corresponding to the peak efficiency (42%) was exhibited in domain II at 1100 °C and  $0.1 \text{ s}^{-1}$  (Fig. 11a). The austenite grain was found to be equiaxed with a finer austenitic grain size of  $18.6 \pm 1.3 \mu\text{m}$ , which was expected to achieve a good trade-off between strength and toughness. Specifically, the well-developed DRX structure was responsible for the high efficiency value according to DMM and brings about grain refinement and deformation resistance reduction in practical steel rolling (Ref 32).

The efficiency of power dissipation at 1100 °C and  $0.001 \text{ s}^{-1}$  as shown in Fig. 9(d) was lower, with merely 16%. In this case, the CDRX in ferrite proceeded more adequately and could decrease the density of intracrystalline defects, thus causing the reduced nucleation rate of austenite and facilitating its boundary migration and growth (Ref 14). As seen from Fig. 11(b), partial recrystallized grains further coarsened to  $64.7 \pm 26.7 \mu\text{m}$ , which must be detrimental to hot working (Ref 33).

The deformation temperatures between 800 and 875 °C and strain rates above  $0.05 \text{ s}^{-1}$  fell into the instability area *A* (see Fig. 9d). As displayed by the specimen deformed at 800 °C and  $10 \text{ s}^{-1}$  (Fig. 12a), some grains were heavily elongated, with a considerable higher fraction of  $\kappa$ -carbides mixed with some finer recrystallized grains nearby the interface of austenite and ferrite. In this case, the grain boundary decohesion induced by the brittle and inter-granular  $\kappa$ -carbide particles would give rise to the localized plastic deformation caused by stress concentration (Ref 37), leading to the particle cracking, interface debonding and the formation of voids (Fig. 12b). The microcracks were connected and further prorogated to the surface of the deformed specimen, causing the macro-damage with an angle of  $45^\circ$  to the compression axis (Fig. 12c–e). The above-mentioned fracture was consistent with the instability area *A* predicted in processing maps.

Similarly, the instability area *B* corresponded to the deformation temperature and the strain rate ranges of 950–1100 °C and  $1\text{--}10 \text{ s}^{-1}$  (see Fig. 9d). As an example, the microstructure 1000 °C and  $1 \text{ s}^{-1}$  was characterized using EBSD, as illustrated in Fig. 13. In general, material did not get enough time to dissipate the adiabatic heat generated during high-strain-rate deformation (Ref 34). The local temperature rose and large amount of stored deformation energy led to the occurrence of necklace dynamic recrystallization (Ref 38), as demonstrated in Fig. 13(a). The necklace structure facilitated inhomogeneous deformation and flow localization nearby the grain boundaries (Ref 23, 38). Meanwhile, there existed some deformed austenite grains with an extremely large size of 86  $\mu\text{m}$  (see Fig. 13b and c), which deteriorated the workability of Fe-11Mn-10Al-0.9C steel.

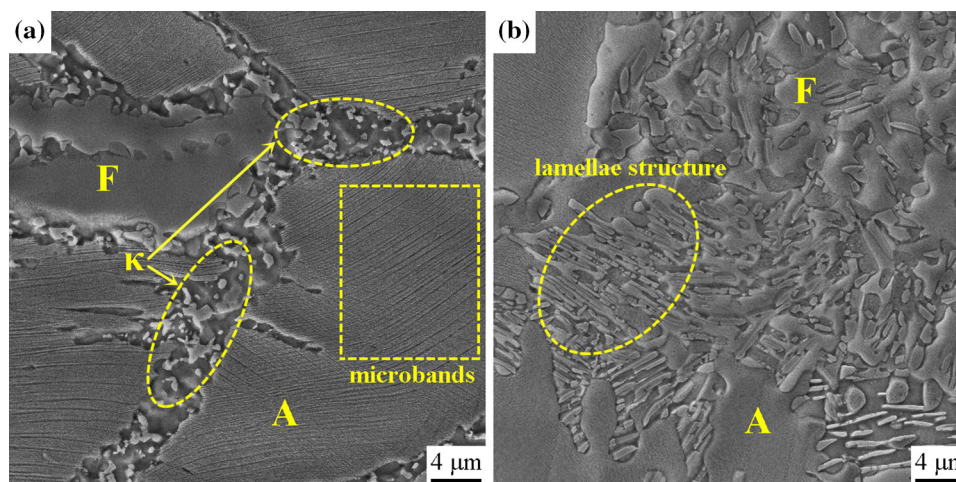


**Fig. 10** SEM micrographs corresponding to the Domain I where the coarsen of  $\kappa$ -carbide leading to high efficiency, with specimens deformed at (a) 800 °C and  $0.01 \text{ s}^{-1}$ , (b) 800 °C and  $0.001 \text{ s}^{-1}$  (A: austenite, F: ferrite,  $\kappa$ :  $\kappa$ -carbide)



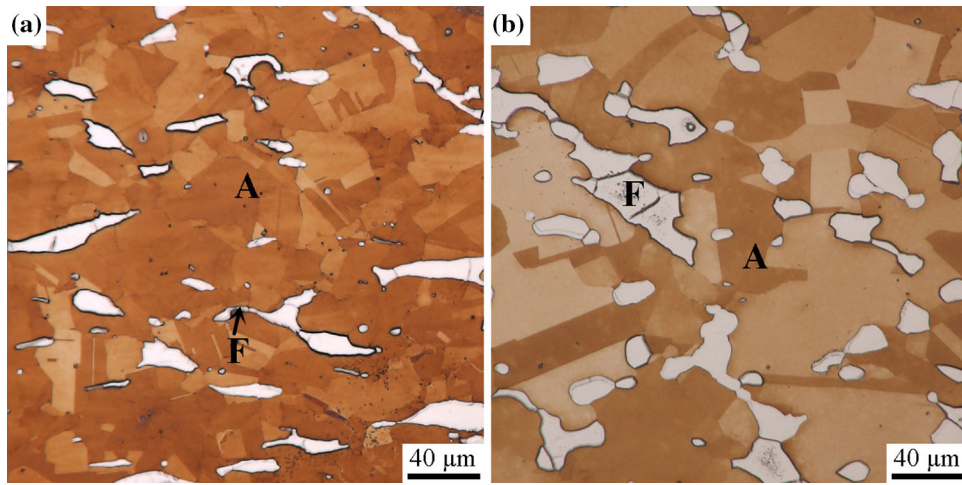


**Fig. 11** (a) OM micrograph corresponding to Domain II with the specimen deformed at 1100 °C and  $0.1 \text{ s}^{-1}$  showing a fine and uniform DRX microstructure, and (b) the excessive growth of DRX grains of size about  $64.7 \pm 26.7 \mu\text{m}$  at high deformation temperature and low strain rate condition indicated by OM micrograph of the specimen deformed at 1100 °C and  $0.001 \text{ s}^{-1}$  (A: austenite, F: ferrite)

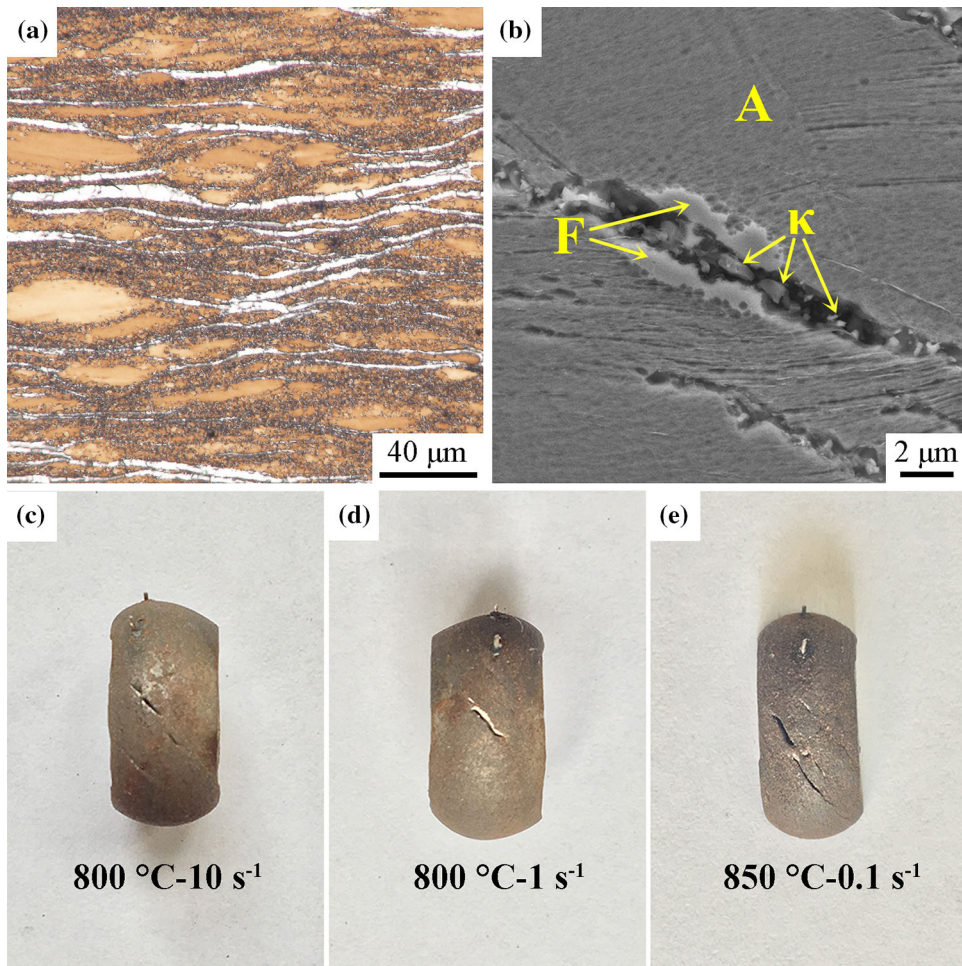


**Fig. 12** Typical microstructure corresponding to the instability area A, with (a) OM micrograph and (b) micro-crack SEM micrograph of the specimen deformed at 800 °C and  $0.001 \text{ s}^{-1}$ , macro-crack morphologies of the specimens deformed at unstable regimes (c-d) (A: austenite, F: ferrite)

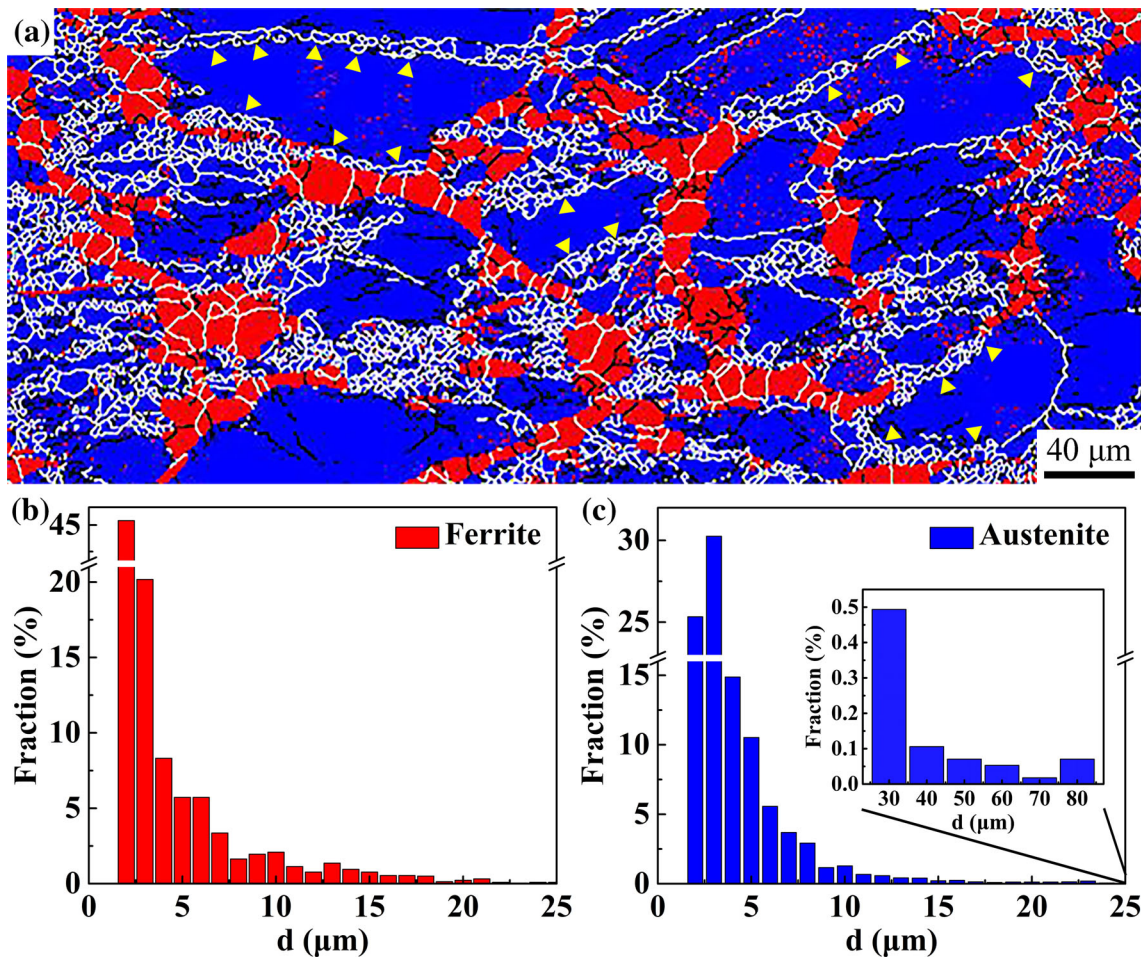


**Fig. 13** The necklace structure corresponding to the instability area B shown by (a) EBSD map of the specimen deformed at 1000 °C and  $1 \text{ s}^{-1}$ , grain size distribution of (b) ferrite and (c) austenite indicating an inhomogeneous microstructure

#### 4. Conclusions

The hot deformation behavior of a Fe-11Mn-10Al-0.9C medium-Mn duplex low-density steel was investigated using hot compression tests at temperatures of 800-1100 °C and strain rates ranging from 0.001 to  $10 \text{ s}^{-1}$ . The main conclusions are as follows:

1. The flow curves can be roughly grouped into two types, involving extensive softening with no apparent steady state at lower temperatures ( $\leq 900 \text{ °C}$ ) and typical DRX with a gradual fall after a peak, followed by a steady state at higher temperatures ( $\geq 950 \text{ °C}$ ).
2. The two distinct flow behaviors were explained based on the detailed microstructural characterization: At lower deformation temperatures, significant softening was mainly attributed to the CDRX of a high-fractioned ferrite together with austenite decomposing into ferrite and inter-granular  $\kappa$ -carbides. At high deformation temperatures, DRX of a high-fractioned austenite was a dominant restoration mechanism.
3. The constructed processing maps of Fe-11Mn-10Al-0.9C steel at various strains were characterized by two efficiency domains. Domain I was located at 800-950 °C and low strain rates,  $< 0.03 \text{ s}^{-1}$ , with a maximum efficiency peak over 68% as a result of the formation and

coarsening of inter-granular  $\kappa$ -carbides. Domain II was located at 1030-1100 °C and strain rates of 0.03- $1.0 \text{ s}^{-1}$  with a peak efficiency of 42%, which was beneficial to obtaining the fine and homogeneous microstructure.

4. The two instability regions in processing maps were presented for the present Fe-11Mn-10Al-0.9C steel. The instability region A appeared at 800-875 °C and strain rates above  $0.05 \text{ s}^{-1}$ , as a result of the formation of inter-granular  $\kappa$ -carbides. The instability region B was located at 950-1100 °C and strain rates of 1- $10 \text{ s}^{-1}$  as a result of heterogeneous necklace structure due to the partial DRX.

#### Acknowledgment

This work was financially supported by the Natural and Scientific Foundation of China (Grant No. 51474062 & U1760205).

#### References

1. S.S. Sohn, H. Song, B. Suh, J.H. Kwak, B.J. Lee, N.J. Kim, and S. Lee, Novel Ultra-High-Strength (Ferrite + Austenite) Duplex Lightweight Steels Achieved by Fine Dislocation Substructures (Taylor Lattices)

- Grain Refinement, and Partial Recrystallization, *Acta Mater.*, 2015, **96**, p 301–310
2. H. Song, J. Yoo, S.H. Kim, S.S. Sohn, M. Koo, N.J. Kim, and S. Lee, Novel Ultra-High-Strength Cu-Containing Medium-Mn Duplex Light-weight Steels, *Acta Mater.*, 2017, **135**, p 215–225
  3. N. Kiskun, A. Sarkar, K.K. Ray, and S. Mandal, Development and Characterization of a Novel Ti-Modified High-Si Medium-Mn Steel Possessing Ultra-High Strength and Reasonable Ductility After Hot Rolling, *J. Mater. Eng. Perform.*, 2018, **27**, p 4077–4089
  4. L. Zhang, X. Huang, Y. Wang, Y. Guo, G. Dai, and D. Li, Achieving Excellent Strength-Ductility and Impact Toughness Combination by Cyclic Quenching in Medium Mn TRIP-Aided Steel, *J. Mater. Eng. Perform.*, 2018, **27**, p 5769–5777
  5. K. Choi, C. Seo, H. Lee, S.K. Kim, J.H. Kwak, K.G. Chin, K.T. Park, and N.J. Kim, Effect of Aging on the Microstructure and Deformation Behavior of Austenite Base Lightweight Fe-28Mn-9Al-0.8C Steel, *Scripta Mater.*, 2010, **63**, p 1028–1031
  6. G. Frommeyer and U. Brüx, Microstructures and Mechanical Properties of High-Strength Fe-Mn-Al-C Light-Weight TRIPLEX Steels, *Steel Res. Int.*, 2006, **77**, p 627–633
  7. W.K. Choo, J.H. Kim, and J.C. Yoon, Microstructural Change in Austenitic Fe-30.0 wt%Mn-7.8 wt%Al-1.3 wt%C Initiated by Spinodal Decomposition and Its Influence on Mechanical Properties, *Acta Mater.*, 1997, **45**, p 4877–4885
  8. D. Liu, M. Cai, H. Ding, and D. Han, Control of Inter/Intra-Granular  $\kappa$ -Carbides and Its Influence on Overall Mechanical Properties of a Fe-11Mn-10Al-1.25C Low Density Steel, *Mater. Sci. Eng., A*, 2018, **715**, p 25–32
  9. S.Y. Han, S.Y. Shin, S.G. Lee, N.J. Kim, J.H. Kwak, and K.G. Chin, Effect of Carbon Content on Cracking Phenomenon Occurring during Cold Rolling of Three Light-weight Steel Plates, *Metall. Mater. Trans. A*, 2012, **42**, p 138–146
  10. S.S. Sohn, B.-J. Lee, S. Lee, and J.-H. Kwak, Effects of Aluminum Content on Cracking Phenomenon Occurring during Cold Rolling of Three Ferrite-Based Lightweight Steel, *Acta Mater.*, 2013, **61**, p 5626–5635
  11. J.D. Yoo and K. Park, Microband-Induced Plasticity in a High Mn-Al-C Light Steel, *Mater. Sci. Eng., A*, 2008, **496**, p 417–424
  12. O.A. Zambrano, J. Valdés, Y. Aguilar, J.J. Coronado, S.A. Rodríguez, and R.E. Logé, Hot Deformation of a Fe-Mn-Al-C Steel Susceptible of  $\kappa$ -Carbide Precipitation, *Mater. Sci. Eng., A*, 2017, **689**, p 269–285
  13. B.H. Sun, H. Aydin, F. Fzaeli, and S. Yue, Microstructure Evolution of a Medium Manganese Steel during Thermomechanical Processing, *Metall. Mater. Trans. A*, 2016, **47**, p 1782–1791
  14. Y.P. Li, R.B. Song, E.D. Wen, and F.Q. Yang, Hot Deformation and Dynamic Recrystallization Behavior of Austenite-Based Low-density Fe-Mn-Al-C Steel, *Acta Metall. Sin. (Engl. Lett.)*, 2016, **29**, p 441–449
  15. T. Siegmund, E. Werner, and F.D. Fischer, On the Thermomechanical Deformation Behavior of Duplex-Type Materials, *J. Mech. Phys. Solids*, 1995, **43**, p 495–532
  16. A. Mohamadizadeh, A. Zarei-Hanzaki, H.R. Abedi, S. Mehtonen, and D. Porter, Hot Deformation Characterization of Duplex Low-density Steel through 3D Processing Map Development, *Mater. Charact.*, 2015, **107**, p 293–301
  17. P. Cizek, The Microstructure Evolution and Softening Processes during High Temperature Deformation of a 21Cr-10Ni-3Mo Duplex Stainless Steel, *Acta Mater.*, 2016, **106**, p 129–143
  18. M.C. Li, H. Chang, P.W. Kao, and D. Gan, The Effect of Mn and Al Contents on the Solvus of  $\kappa$  Phase in Austenitic Fe-Mn-Al-C Alloys, *Mater. Chem. Phys.*, 1999, **59**, p 96–99
  19. R. Raj, Development of a Processing Map for Use in Warm-forming and Hot-forming Processes, *Metall. Trans. A*, 1981, **12**, p 1089–1097
  20. K.A. Babu, S. Mandal, C.N. Athreya, B. Shakthipriya, and V.S. Sarma, Hot Deformation Characteristics and Processing Map of a Phosphorous Modified Super Austenitic Stainless Steel, *Mater. Design*, 2017, **115**, p 262–275
  21. M.K. Mishra, I. Balasundar, A.G. Rao, B.P. Kashyap, and N. Prabhu, On the High Temperature Deformation Behaviour of 2507 Super Duplex Stainless Steel, *J. Mater. Eng. Perform.*, 2017, **26**, p 802–812
  22. N. Park, A. Shibata, D. Terada, and N. Tsuji, Flow Stress Analysis for Determining the Critical Condition of Dynamic Ferrite Transformation in 6Ni-0.1C Steel, *Acta Mater.*, 2013, **61**, p 163–173
  23. W. Zhang, S. Sun, D. Zhao, B. Wang, Z. Wang, and W. Fu, Hot Deformation Behavior of a Nb-containing 316LN Stainless Steel, *Mater. Design*, 2011, **32**, p 4173–4179
  24. D. Ponge and G. Gottstein, Necklace Formation during Dynamic Recrystallization: Mechanisms and Impact on Flow Behavior, *Acta Mater.*, 1998, **46**, p 69–80
  25. A. Momeni and K. Dehghani, Hot Working Behavior of 2205 Austenite-Ferrite Duplex Stainless Steel Characterized by Constitutive Equations and Processing Maps, *Mater. Sci. Eng., A*, 2011, **528**, p 1448–1454
  26. F.J. Humphreys and M. Hatherly, *Recrystallization and Related Annealing Phenomena*, 2nd ed., Elsevier Science, New York, 2004
  27. B. Eghbali, Effect of Strain Rate on the Microstructural Development through Continuous Dynamic Recrystallization in a Microalloyed Steel, *Mater. Sci. Eng., A*, 2010, **527**, p 3402–3406
  28. Y.V.R.K. Prasad, T. Seshacharyulu, S.C. Medeiros, and W.G. Frazier, Effect of Prior  $\beta$ -Grain Size on the Hot Deformation Behavior of Ti-6Al-4 V: Coarse vs Coarser, *J. Mater. Eng. Perform.*, 2000, **9**, p 153–160
  29. S.A. Sajjadi, A. Chaichi, H.R. Ezatpour, A. Maghsoudlou, and M.A. Kalaie, Hot Deformation Processing Map and Microstructural Evaluation of the Ni-Based Superalloy IN-738LC, *J. Mater. Eng. Perform.*, 2016, **25**, p 1269–1275
  30. Y. Lou, H. Chen, C. Ke, and M. Long, Hot Tensile Deformation Characteristics and Processing Map of Extruded AZ80 Mg Alloys, *J. Mater. Eng. Perform.*, 2014, **23**, p 1904–1914
  31. Y. Xiao, H. Liu, D. Yi, J. Le, H.Z. Jiang, X. Zhao, Z. Chen, J. Wang, and Q. Gao, High-Temperature Deformation Behavior of Ti-6Al-2Sn-4Zr-2Mo Alloy with Lamellar Microstructure Under Plane-Strain Compression, *J. Mater. Eng. Perform.*, 2018, **27**, p 4941–4954
  32. E. Pu, W. Zheng, J. Xiang, Z. Song, and J. Li, Hot Deformation Characteristic and Processing Map of Superaustenitic Stainless Steel S32654, *Mater. Sci. Eng., A*, 2014, **598**, p 174–182
  33. S. Tan, Z. Wang, S. Cheng, Z. Liu, J. Han, and W. Fu, Processing Maps and Hot Workability of Super304H Austenitic Heat-Resistant Stainless Steel, *Mater. Sci. Eng., A*, 2009, **517**, p 312–315
  34. Y.V.R.K. Prasad and T. Seshacharyulu, Modelling of Hot Deformation for Microstructural Control, *Int. Mater. Rev.*, 1998, **43**, p 243–258
  35. R. Ebrahimi and A. Najafizadeh, A New Method for Evaluation of Friction in Bulk Metal Forming, *J. Mater. Process. Tech.*, 2004, **152**, p 136–143
  36. J. Seol, D. Raabe, P. Choi, H.S. Park, J.H. Kwak, and C.G. Park, Direct Evidence for the Formation of Ordered Carbides in a Ferrite-Based Low-Density Fe-Mn-Al-C Alloy Studied by Transmission Electron Microscopy and Atom Probe Tomography, *Scripta Mater.*, 2013, **68**, p 348–353
  37. H. Ahamed and V. Senthilkumar, Hot Deformation Behavior of Mechanically Alloyed Al<sub>60</sub>63/0.75Al<sub>2</sub>O<sub>3</sub>/0.75Y<sub>2</sub>O<sub>3</sub> Nano-Composite—A Study Using Constitutive Modeling and Processing Map, *Mater. Sci. Eng., A*, 2012, **539**, p 349–359
  38. M. Jafari and A. Najafizadeh, Correlation Between Zener-Hollomon Parameter and Necklace DRX during Hot Deformation of 316 Stainless Steel, *Mater. Sci. Eng., A*, 2009, **501**, p 16–25

**Publisher's Note** Springer Nature remains neutral with regard to jurisdictional claims in published maps and institutional affiliations.